# Characterization of Additively Manufactured Fuel Grains for Hybrid Rocket Applications

Lance S. Mayhue[1], Jenna M. Matus[2], and Jacob J. Davies[3]
*University of Southern California, Los Angeles, CA, 90007, United States*

**Hybrid rocket motors are significantly less studied than solid and liquid propulsion systems but have great potential for the needs of the next generation of space exploration. They are safe and storable like solids but offer better performance, and they offer the throttleability and control of liquids without the complexity and cost. Hybrids keep their fuel in solid grains, but the traditional casting and curing manufacturing process imposes limits on the shape and therefore performance possible from them. Additive manufacturing provides a fast and cheap means to create complex higher-performing geometries with a new set of 3D printable materials. Small scale experiments of 3D printed hybrid fuel grains have been performed, but a thorough comparison between the performance of these materials and a traditional hybrid grain has not been done yet. This project intends to expand on this existing research by characterizing the regression rate and thrust of different 3D printed grains using ABS as the filament in a laboratory-scale hybrid rocket motor. Five different geometries of ABS fuel grains (including both straight and helical ports) were fired in a hybrid engine that used gaseous oxygen as the oxidizer, ignited by an e-match. The first phase of testing was completed using a setup that gathered chamber pressure data and temperature data on the exterior of the combustion chamber. However, pressure data from the ABS grains was significantly lower than literature surrounding the HTPB grains. Although other studies have demonstrated that ABS may perform similarly to HTPB, this particular setup did not achieve comparable performance due to factors such as nozzle ablation and low oxidizer mass flow rate. However, this project is undergoing a second phase of testing with an improved setup and enhanced data acquisition capabilities to achieve more meaningful results. By including thrust and oxidizer mass flow rate data as well as a fully automated test sequence, the ongoing second stage of the project aims to successfully fire a hybrid rocket motor with multiple grain geometries, giving a basis for further investigation of 3D printed hybrid rocket fuels.**

## I. Introduction

The last decade has seen unprecedented development in the space industry including space tourism, propulsively landed rockets, and future ambitions to return to the moon and set foot on Mars. With these goals comes a need for innovative concepts in propulsion to fulfill the diverse set of requirements of such missions. Casting solid grain prepollent, although effective, does have limitations when it comes to complex grain geometry. Liquid rockets on the other hand, are intrinsically more complicated and thus more expensive. Hybrid rocket propulsion systems are a lesser studied architecture than the traditionally used solid and liquid propulsion systems, but they have several key advantages that merit further research- one being the ability to be manufactured additively for greater flexibility in grain geometry.

Hybrid rocket motors use one component of propellant stored in the solid phase, and the other component stored in a liquid or gaseous phase. Because the fuel and oxidizer are stored separately, the system is safer to manufacture

---

[1] Undergraduate student, Department of Astronautical Engineering, student member

[2] Undergraduate student, Department of Aerospace and Mechanical Engineering, student member

[3] Undergraduate student, Department of Aerospace and Mechanical Engineering, student member

via 3D printing and operate without a significant explosion risk. The safety and storability of hybrids also makes them well-suited for missions to Mars.

Typically, hybrid grains are made of polymer solid fuels such as hydroxyl-terminated polybutadiene (HTPB), which are manufactured by labor and cost-intensive casting processes. Recent advances in additive manufacturing enable a new set of materials and the ability to fabricate complex geometries. Several experiments have demonstrated the capabilities of 3D printed Acrylonitrile Butadiene Styrene (ABS) as an alternative to HTPB fuel grains with success. Data showed that regression rate and specific impulse of ABS were comparable to but slightly lower than HTPB. However, design of helical ports has been validated and shows improvement in ABS regression rates, suggesting potential for geometrical variation to improve the deficiencies of ABS as a hybrid fuel.

To that end, the proposed project will seek to improve on these deficiencies and advance current knowledge in 3D printing of fuel grains by characterizing the performance of ABS in various geometries possible only through additive manufacturing. These geometries include a helical and helical-star grain geometry (a helix with a star cross section), as well as traditional cylindrical and star port grains to be used as a benchmark. Our project attempts to compare HTPB and ABS as hybrid fuel materials to determine if complex 3D printable geometries provide ABS enough advantage to meet or exceed the performance of HTPB in terms of obtainable thrust from same-sized fuel grains. It is known that HTPB will outperform ABS for a regular cylindrical port grain, but our objective is to answer the question, "will the increased burn area and regression rate from the helical-star ABS grain be enough to outperform the traditional straight star port HTPB grain of the same size?"

## II. Theory

The design of the hybrid engine was planned around 3 main objectives: (1) scaling it comparably to other lab studies of small-scale 3D printed grains, (2) choosing design parameters that can be achieved with commercially available equipment while meeting safety requirements, and finally, (3) making a motor that would produce observable changes in chamber pressure (as an indicator of thrust), and regression rate in order to meet the research objective of evaluating performance of ABS vs HTPB.

This model relies on several key assumptions to simplify the design process and predictions, including the ideal rocket assumption and optimum expansion of the nozzle. In order to calculate the chamber pressure and regression rate, the specific heat ratio of the products ($\gamma$) must be calculated based on the propellant chemistry for ABS [4]. Gamma for ABS was calculated using NASA Chemical Equilibrium Analysis (CEA). Additionally, by inputting the expansion ratio of the off-the-shelf nozzle, the desired initial chamber pressure of 150 PSI, and the propellant selection, NASA CEA also produced outputs for chamber and exit temperature, which aided in sourcing components of the test stand, namely the chamber and nozzle which would need to withstand the simulated flame temperatures.

**Table 1 NASA CEA Outputs for ABS combustion.**

| NASA CEA Outputs | |
|---|---|
| Mbar | 22.517 g/mol |
| gamma | 1.145 |
| T0 [K] (temp in combustion chamber) | 3444.860 |
| T_exit [K] (temp at nozzle exit) | 2159.22 |

At a high-level view, the model is designed to take the nozzle geometry (which is predetermined because it is sourced from a third party vendor) and properties of the propellant ($\gamma$, gas constant $R$) as inputs, and output the chamber pressure and regression rate over time for defined grain configurations. Because of the highly interdependent nature of rocket dynamic equations, an initial guess for the chamber pressure was used to begin the iteration. Past GOx/ABS hybrid engines at a similar scale found success with a mean chamber pressure of around 150 psi, so this was set as the initial design chamber pressure. This chamber pressure was then used with characteristic velocity $c^*$ – a standard metric of evaluation– equations to determine the total mass flow rate needed to generate that pressure for the given throat area.

NASA CEA also provided outputs for c* v. oxidizer-to-fuel ratio to determine the optimal O/F ratio for this GOx/ABS engine. The following graph was constructed, showing a maximum efficiency at O/F = 1.7.

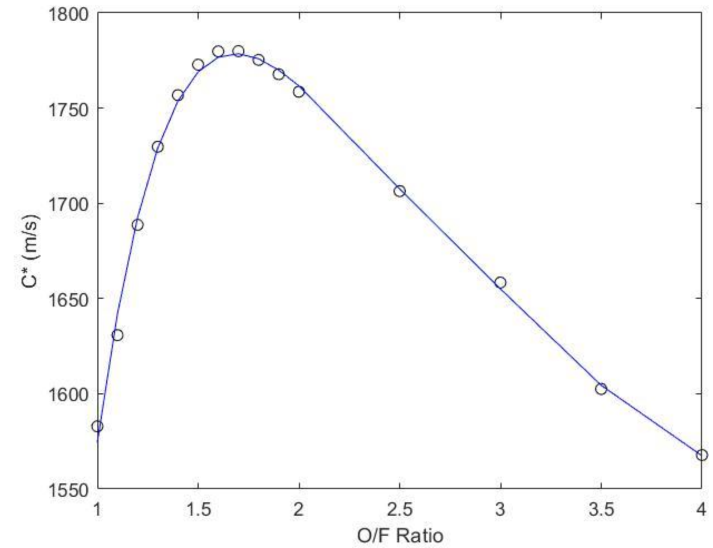

**Fig. 1 C* vs O/F ratio for GOx/ABS, as calculated by NASA's Chemical Equilibrium Analysis software.**

Since the cylindrical port and the helical-cylinder grain have progressive burn profiles, the oxidizer mass flow rate and fuel port diameter were chosen so that the average C* values over the burn (Equation 1) for each grain are as high as possible while maintaining the minimum initial chamber 150 PSI design pressure. This optimization was determined by tracking the O/F ratio throughout the burn using the initial port diameter and estimates for instantaneous regression rate. Tracking the O/F ratio over time ensured that design choices resulted in comparable C* values between the grains.

Instantaneous regression rate predictions were based on a standard equation for hybrid engine regression rate, which is a function of the oxidizer mass flux (mass flow rate / port area). The following equation also includes empirical "burn exponents" from existing literature data on similar sized GOx/ ABS hybrids.

$$\dot{r}_{ABS} = 0.55(G_{ox})^{0.26} \qquad (1)$$

This allows instantaneous regression rates to be calculated for each grain, with the total flow rate (for cylindrical ports) increasing as the regression rate and therefore fuel flow rate increases. This means at each time step, the chamber pressure will also increase to produce the progressive burn profile expected from cylindrical port geometries. Additionally, instantaneous chamber pressure can be calculated by solving the choked flow equation for pressure, resulting in the following equation:

$$P_0 = \frac{\dot{m}}{A^*}\sqrt{\frac{RT_0}{\gamma}}\left(\frac{2}{\gamma+1}\right)^{-\left(\frac{(\gamma+1)}{2(\gamma-1)}\right)} \qquad (2)$$

In Equation 2, mdot is the instantaneous mass flow rate to calculate the instantaneous chamber pressure. Due to budget constraints, this study collects only chamber pressure data, but it is assumed to be a direct indicator of thrust. Assuming Pe = Pa (optimum expansion), the theoretical thrust of the engine is below:

$$F_{th} = P_0 A^* \sqrt{\frac{2\gamma^2}{\gamma-1}\left(\frac{2}{\gamma+1}\right)^{\frac{\gamma+1}{\gamma-1}}\left(1-\left(\frac{P_e}{P_0}\right)^{\frac{\gamma-1}{\gamma}}\right)} \qquad (3)$$

All terms to the right of Po in Equation 3 above are constant except for the ratio of exit to chamber pressure. Assuming chamber pressure will not drastically change during the short burn, and given that the impact of this term is minimized by the fraction exponent, this will also be assumed to be constant. This means that the thrust equation reduces to the chamber pressure multiplied by a constant, validating the use of chamber pressure data as a direct indication of engine thrust performance.

The size of the fuel grains being tested influences the characteristics of the engine and vice versa. We performed iterative calculations to adjust parameters to end up with resulting grain dimensions that were feasible to fabricate with a Creality Ender 3 FDM printer. The inner diameter and grain length were chosen to be .3" and 6" respectively, which were large enough to produce a measurable difference in chamber pressure to calculate thrust, but small enough to be printed in a reasonable time (30 hours with 100% infill density). The outer diameter (2") was chosen based on the predicted regression rate along with a 50% margin (to account for expected amplification with helix grain) to ensure that the motor will not experience burn-through during the firing.

The star grain was chosen for its neutral burn profile, which will allow for a clear comparison between ABS and HTPB. Parameters for the helical ABS grain were chosen based on a top-performing helical grain in a previous study of similar size. The helical grain uses a similar helix ratio while still fitting in the confines of the relatively small grain geometry. Parameters such as pitch distance and helix diameter were chosen to provide a measurable performance boost whilemaintaining manufacturability. Currently, the model calculates chamber pressure based on the run length of the helix centerline, so the helix shape needs to provide a significant amount of additional length to see an increase in chamber pressure.

All four grains share the same oxidizer mass flow rate which will be held constant for the duration of the burn. Because of the limitations of the system including injector and grain sizing, the engine is only set to run at 1 oxidizer mass flow rate. So, the star and star helix grains cannot be optimized at a 1.7 O/F ratio because it would require changing the oxidizer flow rate. However, this experiment just seeks to compare the star vs the helical-star in terms of chamber pressure, and show that the star shape results in a neutral burn, making it easier to set a desired O/F ratio.

The final design parameters for each grain are as follows:
*All grains have constant length (6"), OD (2"), and fuel port area (.071 in^2)

**Table 2 Grain Design Parameters.**

| **Parameter:** | **Cylinder** | **Star** | **Helical-cylinder** | **Helical-star** |
|---|---|---|---|---|
| Expected Initial Chamber Pressure (PSI) | 144.361 | 144.361 | 169.52 | 169.52 |
| Final Chamber Pressure (PSI) | 178.148 | 144.361 | 218.442 | 169.52 |
| C*avg (m/s) | 1655.178 | 1566.877 | 1750.892 | 1680.171 |
| Helix Pitch Length (in) | / | / | 3 | 3 |
| Helix Loop Diameter (in) | / | / | 1 | 1 |

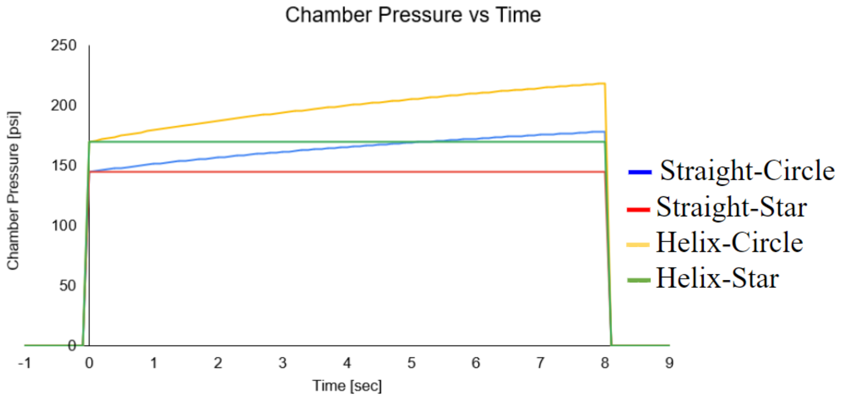

**Fig. 2 Predicted Chamber Pressure Traces for each Grain.**

Based on the grain and nozzle dimensions, oxidizer mass flow rate, and initial chamber pressure, the above equations were used to construct Figure 2, which displays the predicted chamber pressure curves for each grain. The circular cross sections are progressively burning (increasing pressure) while the star cross sections are assumed to have a neutral burn profile. The additional internal surface area of the helical designs effectively gives the fuel grains added port length, which increases the initial chamber pressure. This increased length also increases the skin friction experienced by the propellant flowing through the grain, which adds energy to the flow and increases the regression rate, leading to even higher pressure and thrust. While previous studies have identified skin friction effects, this phenomenon is not accounted for by the model for simplicity. This means the model should underpredict the helical grain performance.

Once the grain geometries were finalized and the chamber pressure throughout the burns was simulated, the injector could be sized to deliver the necessary oxygen flow rate and prevent back flow or oxygen starvation of the combustion chamber. For all burns, the maximum estimated chamber pressure was 218.44 PSI. The literature on injector design recommends a 20% drop in pressure across the injector for unthrottled, and a 30% drop for throttled engine designs. While the oxygen flow rate will be fixed, the progressive nature of the cylindrical ports acts as a throttled engine, so the injector was designed with a 25% pressure drop based on the maximum expected chamber pressure. From these calculations, it was determined that a 1/16" diameter orifice was needed to properly regulate the mass flow rate of the oxidizer.

### A. **Experimental Setup**

The static fire test-stand for this project consisted of two main subassemblies. There was the feedline subassembly where high-pressure gaseous fluids would flow into the combustion chamber subassembly. The combustion chamber houses the different fuel grains that were ignited.

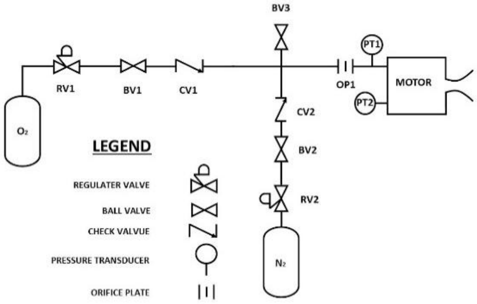

**Fig. 3 Overview schematic diagram of experimental set-up.**

The schematic in Figure 3 shows the overview of the experimental setup and how the feedline was connected to the motor, which represents the combustion chamber. One pressure transducer was installed in the feedline "PT1" as a redundant sensor, and another was installed in the combustion chamber "PT2" as the main source of collecting pressure data in the chamber during combustion. Due to accessibility and budget constraints, MSP300 pressure transducers from TE connectivity were selected for the experiment's data collection. The pressure transducers were rated for pressures up to 15 kpsi and an operating temperature of 85 degree celsius. They also have a 1% span accuracy. Therefore, the selected pressure transducers were compatible with the scope of this project. These pressure transducers were then connected to a National Instruments USB-6211 data acquisition unit.

The feedline subassembly is responsible for delivering high-pressure gaseous oxygen and nitrogen to the combustion chamber. The feedline delivered gaseous oxygen to the chamber when combustion was necessary. When combustion in the chamber needs to be purged for safety precautions or eliminating residual burn, then gaseous nitrogen was introduced into the chamber.

Two K-size gas cylinder tanks carried compressed oxygen and nitrogen gas. Based on the theoretical model and assumptions made, the gas cylinder tanks had to deliver each gas at 275 PSI. Pressure regulators were connected to the tanks to ensure that the pressure of the gas entering the feedline was 275 PSI. Each of the regulators was connected to manual ball valves where an operator controls the flow of each gas. The two separate lines connected to each gas tank had check valves upstream of the cross fitting that merges the two lines. Check valves were used to prevent any backflow towards the gas tanks. On the cross fitting, a drain valve was incorporated to release any unwanted pressure in the feedline. Another important function for the feedline was to control the flow rate of the gas going into the chamber. Since flowmeters were out of the budget, a specifically sized flow control orifice plate was used to allow the desired flow rate of gaseous oxygen into the combustion chamber. Then, a 6" steel pipe nipple replaced nylon tubing right before the chamber so that the gas could enter into the chamber axially. A pressure transducer was also placed in the feedline before the chamber which acted as a redundant and backup sensor to verify readings of the main pressure transducer in the combustion chamber.

### B. Combustion Chamber

The feedline assembly is connected to a combustion chamber assembly where the combustion will take place. The main components as seen in Fig. **4** are two ¾”-thick steel end caps, a ¼”-thick steel pipe, two steel spacers, an NPT adapter, two O-rings, the nozzle, and four 10.5” bolts and related fasteners. Furthermore, a pressure transducer was attached to the combustion chamber using the NPT adapter fastened to the steel pipe.

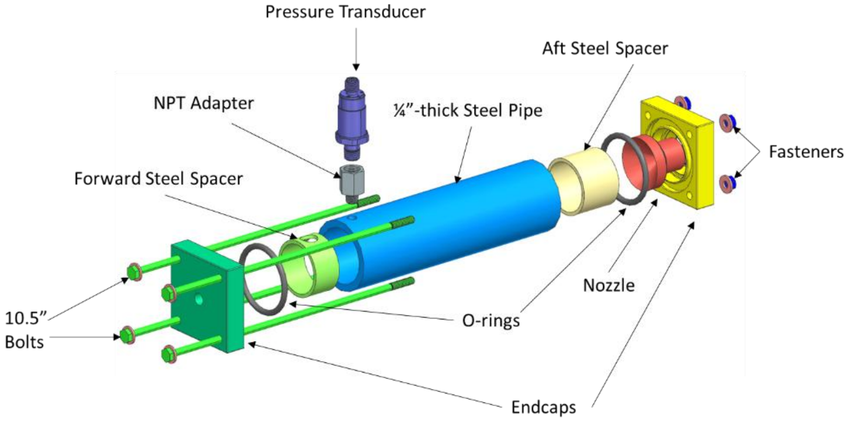

**Fig. 4 Combustion chamber assembly used for the firing of the fuel grains.**

The steel pipe was chosen to be ¼”-thick because that thickness was necessary for thread engagement of the NPT adapter for the pressure transducer. The length and diameter of the steel pipe was based on the fuel grain design. The fuel grains were designed with an outer diameter of 2” and a length of 6”. As a result, the inner diameter of the steel pipe was 2”. For the length of the steel pipe, it was required to consider the length of the pre- and post-combustion areas. For proper combustion to occur, the ratio of the length of the pre- and post-combustion areas to the outer diameter of the fuel grain must be at least 0.5 and 0.75, respectively. This gives the pre-combustion area a length of 1” and the post-combustion area a length of 1.5”. In total, the steel pipe must then be at least 8.5” in length, which was the length used. Relatedly, the length of the spacers must also be the lengths of the pre- and post-combustion areas to ensure that the fuel grain does not move inside the steel pipe.

Data from PTs and thermocouples was collected by utilizing a National Instruments (NI) USB-6211 data acquisition (DAQ) system, and operated via a virtual instrument (VI) file in LabView. Each of the PTs were configured to measure the voltage across the sensor relative to the internal ground of the NI DAQ. The thermocouples were configured utilizing the NI DAQ’s internal thermocouple setup but were calibrated by utilizing external input data gathered by performing a calibration test. All of the sensors were set to continuously measure at 1,000 Hz and raw data from all of the sensors were exported as lvm files to be analyzed in MATLAB. Additionally, the VI was also responsible for controlling the ignition system of the circuit. The ignition system of the circuit consisted of a TIP-120 transistor connected to two 9 volt batteries in parallel at the collector pin, and an e-match connected at the emitter pin. Upon user input, the DAQ would send a small current through the base of the TIP-120 transistor and connect the e-match to the external power supply, thus starting the combustion cycle.

## III. Results

A series of four static fires was executed, one for each of the four geometries described above. Chamber pressure was recorded by the redundant PTs, and the fuel grain mass and port diameter, as well as the nozzle throat diameter, were measured before and after each firing for comparison to the model and assessment of its assumptions. The following figures show the pressure and thrust traces of each grain over the course of the firing, which lasts about 20 seconds from startup to full shutdown. While the shape of the pressure traces are similar to our expectations from the model, the magnitudes are five to ten times lower than the model predictions. While the model predicted initial pressures of 144.4 and 169.5 PSI for the straight and helical ports respectively, the initial chamber pressures were around 26 PSI for the nominal firings such as the circle helix test shown in Figure 5. Pressure Transducer uncertainty is determined by its resolution, which is ± 1% of the output pressure value.

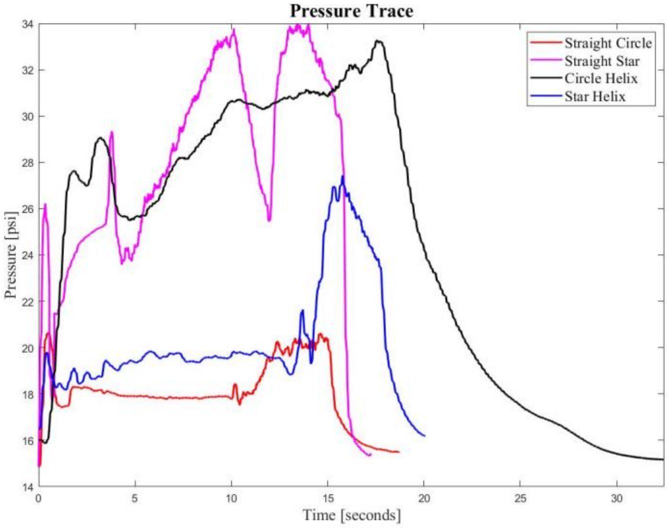

**Fig. 5 Overlay of pressure trace for each of the four grain geometries.**

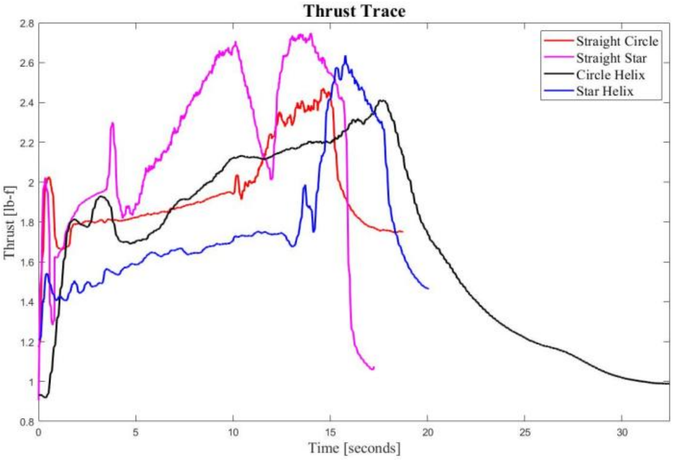

**Fig. 6 Overlay of Thrust Data for each grain geometry.**

There are a couple of important things to note about these static fires besides the significant underperformance of the engine. First, there is a large dip in the pressure and thrust traces for the straight star grain around 10 seconds into the firing. This is due to an experimental error in which the operator of the compressed gas cylinders paused a few seconds after shutting off the oxygen line and opening the nitrogen line. Once the oxygen was shut off, the pressure rapidly fell until the nitrogen line was opened and reestablished the 275 psi back-pressure to push the remaining oxygen in the line through the combustion chamber. Second, the star helix firing was a partial ignition. While the grain lit and continuous combustion occurred, the engine experienced difficulty reaching full and steady ignition. Video recording of the firing demonstrates a long period of chugging with more smoke and a smaller, less intense flame in comparison to the other firings until the grain begins to fully ignite towards the end of its firing. This explains the strange behavior seen in the graphs above of mostly low performance with a rapid spike in chamber pressure towards the end of the star helix firing. Measurements were also taken by hand before and after each firing to collect data on the mass, port diameter, and the throat diameter of the nozzle. These measurements are summarized in Table 3 below for each of the four grains.

Table 3 Grain Measurements Taken Before and After Firing.

| Shape | Density [g/cm^3] | Initial Mass [g] | Final Mass [g] | Initial Throat Diameter [in] | Final Throat Diameter [in] | Initial Port Diameter [in] | Final Port Diameter [in] |
|---|---|---|---|---|---|---|---|
| Circle Helix | 0.877 ± .003 | 263 ± 1 | 215 ± 1 | 0.185 ± .001 | 0.202 ± .001 | 0.276 ± .001 | 0.63 ± .001 |
| Straight Star | 0.877 ±.003 | 265 ± 1 | 246 ± 1 | 0.202 ± .001 | 0.206 ± .001 | 0.276 ± .001 | 0.49 ± .001 |
| Star Helix | 1.004 ± .003 | 301 ± 1 | 279 ± 1 | 0.206 ± .001 | 0.230 ± .001 | 0.276 ± .001 | 0.42 ± .001 |
| Straight Circle | 0.911 ± .003 | 275 ± 1 | 263 ± 1 | 0.230 ± .001 | 0.262 ± .001 | 0.276 ± .001 | 0.46 ± .001 |

## IV. Discussion

### A. Nozzle Ablation

After the first nominal firing, ablation of the nozzle throat became noticeable. To account for this, measurements were taken with gauge pins to determine the nozzle throat diameter before and after each firing. Unfortunately, as seen in Table 3, the glass phenolic nozzle started at a throat diameter of .185" and had expanded to .262" by the end of the last firing. As the throat area increases, it is expected that chamber pressure will decrease, according to Equation 2. This agrees with what was recorded in the latter two fires- the star helix, and the straight circle- which exhibited lower chamber pressures than their previously fired counterparts. In Figure 6, the overlaid thrust traces show very similar profiles, excluding the star helix which was a bit lower due to having only partial ignition. The maximum thrust achieved from the experiment was 2.74 lbf, which is about 5.4 times less than the expected maximum thrust of 14.81 lbf predicted by the original model.

### B. Incorrect Oxidizer Mass Flow Rate

While the effects of nozzle ablation clearly impacted the engine's performance and could explain variation between firings, it does not account for the large difference between the expectations of the model and experimental results, especially for the first and second firing when nozzle ablation was minimal, and the throat diameter was closer to the nominal value. The most likely source of this discrepancy is the lack of measurement and control of the oxygen flow rate from the flow control orifice. Typical liquid or hybrid engines use a dedicated flowmeter or an orifice plate with a differential pressure transducer in the feedline, which can be combined with a controlled throttleable valve to maintain a constant, measured flow rate at the desired value like the model assumed. The pressure data was imported to MATLAB for analysis to determine the approximate mass flow rate and to test the validity of the equations used in the model by comparison of the predicted final mass and port diameters to the measured results. The first step was to calculate the estimated thrust, as plotted in the figures above, using Equation 3. For any rocket, the thrust can be given by

$$F_{Th} = \dot{m} g_0 Isp \quad (4)$$

Where mdot is the total mass flow rate, Isp is the specific impulse, calculated to be 217-247 seconds at sea level using NASA's Chemical Equilibrium Analysis (CEA) software with known engine parameters, and g is the gravitational constant. Using the calculated thrust and the Isp outputs from CEA, the time-varying total mass flow rate was calculated. Because the total mass flow rate is the sum of the oxygen and fuel mass flow rates, and the fuel mass flow rate is itself a function of the oxygen mass flow rate according to regression rate Equation 1, the instantaneous oxygen mass flow rate can be calculated given a known port diameter, port length, and grain density. The instantaneous port diameter needed in this calculation was found at every time step by integrating the regression rate up to the current time step starting from the measured initial port diameter given for each grain in Table 3. A sample regression rate plot used in this calculation is shown below.

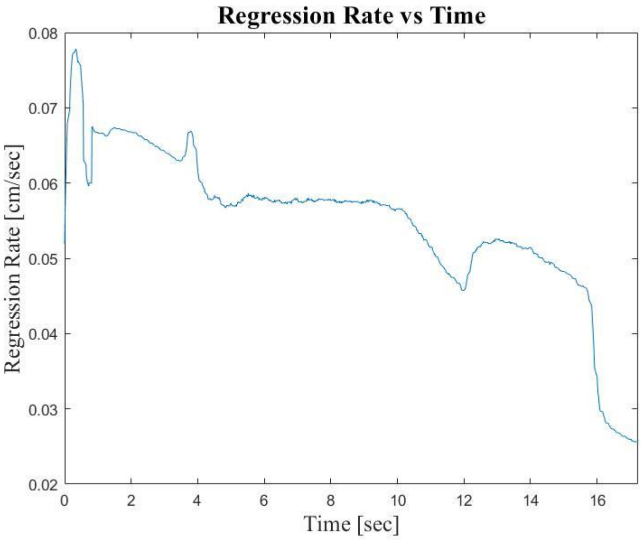

**Fig. 7 Semi-Theoretical Regression Rate Calculation for Straight Star Grain.**

This regression rate plot, as well as a similar plot of the total fuel mass flow rate, can be integrated over the burn duration to yield the final port diameter and mass, respectively, predicted by the model equations for each grain.The model is validated if these predictions match what was measured after the firings. In that case, the issue is shown to be with the hardware's inability to create the desired test conditions rather than with the model's inadequacy in describing the physical behavior of the system. When the regression rate and fuel mass flow rate data was integrated using the original regression rate formula taken from literature, the predicted values deviated significantly from the measured values. This led to suspicion that the empirically-determined burn coefficient ($a = 0.055$) and burn exponent ($b = 0.260$) taken from a previous study were inaccurate. By heuristically varying these values to $a = 0.032$ and $b = 0.120$, much more accurate predictions were made, as shown in Table 4.

**Table 4 Comparison of Literature and Heuristic Manipulation Models to Estimate Total Mass Loss and Final Port Diameter.**

| Grain Type | Mass Lost (literature model) [g] | Mass loss Error (literature model) | Mass Lost (heuristic model) [g] | Mass loss Error (heuristic model) | Final Port Dia. (literature model) [in] | Final Port Dia. Error (literature model) | Final Port Dia. (heuristic model) [in] | Final Port Dia. Error (heuristic model) |
|---|---|---|---|---|---|---|---|---|
| Circle Helix | 62 | 29.00% | 46 | 4.05% | 0.832 | 32.13% | 0.731 | 16.08% |
| Straight Star | 35 | 84.28% | 20 | 2.87% | 0.728 | 48.51% | 0.574 | 17.10% |
| Star Helix | 39 | 76.50% | 27 | 24.77% | 0.680 | 62.00% | 0.591 | 40.76% |
| Straight Circle | 38 | 212.99% | 21 | 76.72% | 0.750 | 63.04% | 0.592 | 28.76% |

In all cases, the percent difference between the prediction and the measurement significantly improved, and in some cases this improvement was drastic. For example, the literature regression model incorrectly predicted the mass by 84.28% while the heuristically determined regression model was only off by 2.87%. Sometimes, the new heuristic model still deviated significantly as in the case of the straight circle mass loss (76.72%, though this is vastly better than the literature model error of 212.99%). An even more accurate model could be created by determining a and b mathematically from a series of more reliable datasets rather than the heuristic method used here. The point, however, is that even with the limited data available which was taken with inconsistent test conditions (e.g., different levels of ignition, manually controlled valves), the model can largely make reasonable predictions of the measured mass and port diameter -- strong evidence that the fundamental relationships implemented in the model are accurate. This suggests the large discrepancy between expected and experimental chamber pressure is due to the inaccuracy of the flow control orifice, not with the model used.

The total mass flow rate, the oxygen mass flow rate, and the fuel mass flow rate were calculated for each grain using the method described previously, and each grain produced plots similar to the figures below. The results using the literature regression rate model are shown along with the results of the heuristic regression rate model for comparison. Note that the literature model calculates a consistently higher fuel mass flow rate, which would yield an O/F ratio less than unity, whereas the heuristic model calculates a higher oxygen mass flow rate with the O/F ratio around two, approximately where the engine was designed to operate.

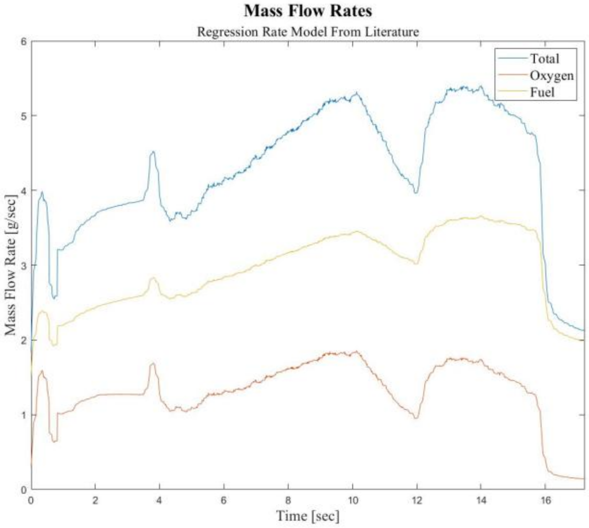

**Fig. 8 Mass Flow Rates of Straight Star Grain Predicted by Literature Regression Rate Formula.**

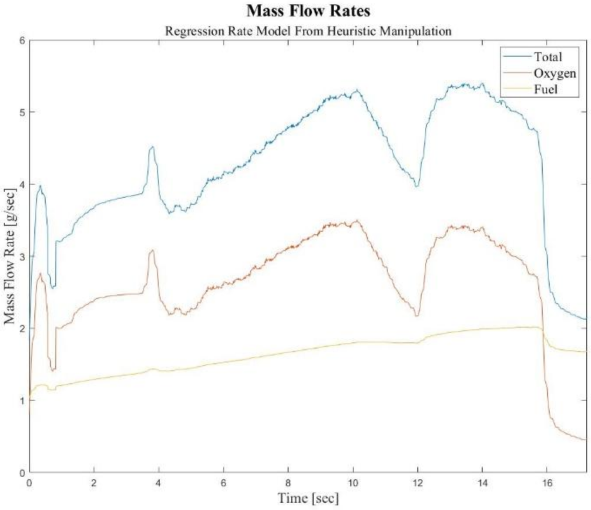

**Fig. 9 Mass Flow Rates of the Straight Star Grain Predicted by Heuristic Regression Rate Formula.**

The key conclusion from these mass flow rate plots is that no matter which regression rate model is used, the oxygen mass flow rate is 1-3 grams per second, which is several times less than the desired minimum of 6 grams per second. Increasing the oxygen flow rate has the additional effect of increasing the fuel flow rate since the two are coupled, which means the total mass flow rate -- which is the driver of thrust and chamber pressure -- would be impacted by improved control over the oxygen mass flow rate. It seems clear from the presented analysis that the key sources of significant error observed in these experiments are primarily due to the inadequate oxygen feedline control and the escalating effects of nozzle ablation obstructing engine performance.

# V. Conclusion

Additively manufacturing grains allow propulsion engineers to explore a wider range of complex geometries that would not be possible using conventional grain casting and manufacturing methods. Helical geometries have the benefit of an increased effective grain length and therefore burning surface area, as well as the posited effect of skin friction. Past research has shown that the induced helical flow pattern causes greater friction against the flow on the grain's burning surface, which increases regression rate and therefore overall mass flow rate. Despite these benefits which would suggest that grains with a helical port would outperform their conventional counterparts, the results produced in this project did not show a significant performance improvement in complex shapes. ABS grain pressure values were 5 times lower than expected values, and grains with helical shapes repeatedly had failed ignitions. The largest thrust value was generated by the straight star grain: 2.74 lbf despite having undergone nozzle ablation and having less burning area compared to the helixes, which is opposite to what was expected.

Since the underperformance seen in the pressure and thrust data may be driven by issues in the feedline system and nozzle ablation, it is difficult and even inappropriate to make any conclusion on the performance of ABS relative to HTPB. Additionally, given the inconsistencies between firings, it is also difficult to draw conclusions on the potential advantages of helical port designs, or the progressiveness vs. neutrality of the burn profiles between the circular and star cross sections.

Rather than attempting to determine thrust indirectly via pressure measurements, a complete thrust stand and load cell would be much more suitable for characterizing these additively manufactured grains. Having a definitive measurement of oxidizer mass flow rate via a venturi or other flow sensor to anchor the regression rate calculations would also be extremely beneficial. At the very least, resizing the orifice is necessary to increase the oxidizer mass flow rate to a more optimal value. Additionally, to better understand the behavior of helical grains, a comprehensive study comparing various helix patterns may prove to shed light on the topic, as the repeated difficulty in lighting the helical grains could be a result of having too aggressive of a helical geometry. Lastly, manufacturing a nozzle out of a more durable material like graphite should improve the trustworthiness of the results for both pressure and thrust models.

# Acknowledgments

The authors thank Dr. Robert Antypas for his advice and project support. Additionally, the authors acknowledge Jeffrey Vargas, Seth Weiman, and the Baum Family Makerspace for project support, manufacturing, and the use of facilities for testing.

# References

[1] Z. S. Spurrier, *Throttleable GOX/ABS Launch Assist Hybrid Rocket Motor for Small Scale Air Launch Platform.* PhD thesis, Utah State University, 2016.

[2] R. A. Chandru, N. Balasubramanian, C. Oommen, and B. N. Raghunandan, "Comparing hydroxyl terminated polybutadiene and acrylonitrile butadiene styrene as hybrid rocket fuels," Journal of propulsion and power, vol. 34, no. 4, pp. 1090–1093, 2018.

[3] S. A. Whitmore, Z. W. Peterson, and S. D. Eilers, "Comparing hydroxyl terminated polybutadiene and acrylonitrile butadiene styrene as hybrid rocket fuels," *Journal of propulsion and power,* vol. 29, no. 3, pp. 582–592, 2013.

[4] M. Gruntman, "Elements of thermodynamics and combustion," in *Rocket and Spacecraft Propulsion: ASTE 470 Notes*, ch. 6, University of Southern California Astronautical Engineering Department, 2021.